Postprint of: Kulpa A., Ryl J., Schroeder G., Koterwa A., Sein Anand J., Ossowski T., Niedziałkowski P., Simultaneous voltammetric determination of Cd2+, Pb2+, and Cu2+ ions captured by Fe3O4@SiO2 core-shell nanostructures of various outer amino chain length, Journal of Molecular Liquids, Vol. 314 (2020), 113677, DOI: 10.1016/j.molliq.2020.113677

Simultaneous voltammetric determination of Cd^{2+}, Pb^{2+}, and Cu^{2+} ions captured by $Fe_3O_4@SiO_2$ core-shell nanostructures of various outer amino chain length

A. Kulpa[1], J. Ryl[2], G. Schroeder[3], A. Koterwa[1], J. Sein Anand[4,5], T. Ossowski[1], P. Niedzialkowski[1]*

[1] Department of Analytical Chemistry, Faculty of Chemistry, University of Gdansk, Wita Stwosza Str. 63, 80-308 Gdansk, Poland

[2] Department of Electrochemistry, Corrosion and Materials Engineering, Faculty of Chemistry, Gdansk University of Technology, Narutowicza 11/12, 80-233 Gdansk, Poland

[3] Faculty of Chemistry, Adam Mickiewicz University in Poznan, Uniwersytetu Poznańskiego Str. 8, 61-614 Poznan, Poland

[4] Department of Clinical Toxicology, Medical University of Gdansk, 4/6 Kartuska St., 80-104 Gdansk, Poland

[5] Pomeranian Center of Clinical Toxicology, 4/6 Kartuska St., 80-104 Gdansk, Poland

*corresponding author: Pawel Niedzialkowski

e-mail address: pawel.niedzialkowski@ug.edu.pl

tel: +48 58 523 51 00

Abstract

In the present study, we examined a novel functionalised magnetic nanoparticles $Fe_3O_4@SiO_2\text{-}N_n$ as a nano adsorbent for binding of Cd^{2+}, Pb^{2+}, Cu^{2+} ions in an aqueous solution. First, we obtained the nanoparticles functionalised with various carbon chains containing different number of amino groups: (3-amino)propyltriethoxysilane ($Fe_3O_4@SiO_2\text{-}N_1$), N-(2-aminoethyl)-3-aminopropyltrimethoxysilane ($Fe_3O_4@SiO_2\text{-}N_2$) and *N*^{1}-(3-trimethoxysilylpropyl)diethylenetriamine ($Fe_3O_4@SiO_2\text{-}N_3$). In the next step, we conducted their characterisation using SEM, TEM, FT-IR, and XPS methods.

The detection of Cd^{2+}, Pb^{2+}, Cu^{2+} metal ions was performed under optimised experimental conditions using DPASV and HDME techniques. Using these methods we conducted the Cd^{2+}, Pb^{2+}, Cu^{2+} binding comparison in 4.5 µM concentration with 4 mg of $Fe_3O_4@SiO_2\text{-}N_n$. Obtained results show that the adsorption rate of each ion differs due to the nanoparticles modification.

The highest Pb^{2+} binding capacity was achieved using $Fe_3O_4@SiO_2\text{-}N_1$ and $Fe_3O_4@SiO_2\text{-}N_2$. The smallest binding capacity was observed for Cd^{2+} ions by $Fe_3O_4@SiO_2\text{-}N_2$ and $Fe_3O_4@SiO_2\text{-}N_1$.

The Cd^{2+} biding was not observed for both $Fe_3O_4@SiO_2\text{-}N_2$ and $Fe_3O_4@SiO_2\text{-}N_3$ nanoparticles. Additionally, Pb^{2+} was not bound by $Fe_3O_4@SiO_2\text{-}N_3$. The research results show that the $Fe_3O_4@SiO_2\text{-}N_3$ nanoparticles bind copper ions with high selectivity.

For the first time we performed the adsorption-desorption experiments using DPASV to prove the Cu^{2+} binding activity of $Fe_3O_4@SiO_2\text{-}N_3$ nanoparticles. Obtained results indicate that examined nanoparticles show strong binding capability. Additionally, we obtained 99.9 % recovery of Cu^{2+} ions.

Keywords: Fe_3O_4 nanoparticles; amino-modified $Fe_3O_4@SiO_2$ nanostructures; cadmium, lead and copper ions removal, copper adsorption-desorption experiment

1. Introduction

In the last few decades we observed increasing heavy metal pollution generated by human activity - manufacturing processes such as refining and use of fertiliser and pesticides. Heavy metals have caused serious environmental concerns due to their low biodegradability, bioaccumulation tendency and mutagenicity [1,2]. Many heavy metals are regarded as carcinogens [3]. Due to the dissemination of lead in the environment and its increasing usage in industry, its carcinogenicity has been an object of interest of many research projects. Based on the experimental carcinogenicity results, the International Agency for Research on Cancer (IARC) commission classified lead and inorganic lead derivatives in 2B group, considered as possible carcinogenic to humans [4], while cadmium is classified as a human carcinogen [5]. Lead does not cause cancer, but it can contribute to its development [6,7]. Cadmium causes cancer by multiple mechanism based on, among others, inhibition of DNA damage repair and oxidative stress [5]. Recycling of heavy metals from wastewater has become essential field of scientific research and industry.

In recent years scientists utilised many metal ion separation and removal methods, including chemical co-precipitation [8], chemical coagulation process [9], flotation [10,11] and microflotation [12] techniques, ion removal by membrane filtration [13], osmosis [14], extraction with ionic liquids [15]. Adsorption methods predominate over traditional separation techniques due to their simplicity, easy handling and sludge-free operation, regeneration capacity, and cost-effectiveness [16]. Many metal ion adsorbents are known, including pumice [17], composite mineral adsorbents [18], pectin-based adsorbents [19], organic frameworks [20], and carbonaceous materials, such as activated carbon [21], biochar [22], carbon nanotubes [23], and graphene oxide [24].

Nowadays, the most popular agents for wastewater ion removal are the superparamagnetic modified nanoparticle adsorbents based on iron oxide Fe_3O_4 — imprinted magnetic biosorbent [25], copolymerized polyacrylamide cellulose modified nanomagnetite [26], sultone-modified magnetic activated carbon for Cd^{2+}, Pb^{2+}, and As^{3+} removal [27], and many magnetic materials used for dye remediation [28–30]. The superparamagnetic Fe_3O_4 nanoparticles with functionalised surface adsorbent have been successfully applied to remove variety of wastewater heavy metal ions, such as copper, zinc, mercury, chromium, lead, cadmium, manganese, uranium, or silver [31–35]. Among adsorbents utilised to remove both organic and inorganic wastewater compounds, magnetic nanoparticles with large surface area, facile maintenance, and high efficiency took a special place due to the simple, convenient, and fast separation using external magnetic field [36–40]. In comparison with the traditional solvent extraction, these superparamagnetic modified nanoparticle adsorption methods are more economic, more cost-effective, and environmentally friendly [41]. Many research groups focused on the amino-functionalised $Fe_3O_4@SiO_2$ core-shell magnetic nanocomposites as a novel adsorbent for the removal of aqueous pollutants [42,43].

Metals like, among others, gadolinum, technetium, iron, manganese, cobalt, gallium, play a crucial role in medicine. These elements are widely used in diagnostic procedures as, for example, radioisotope or contrast agents. Additionally, platinum, gold, silver, lithium, zinc, iron, or bismuth may also be used in a treatment of various diseases [44].

Metals can also be extremely toxic and cause life-threatening illnesses [45]. One of the most frequently occurring disease is Wilson's disease.

Wilson’s disease is a rare, autosomal recessive, and lethal-without-treatment genetic disorder caused by the excessive copper storage in various body tissues. In the case of healthy individuals, we can observe a balance between intestinal absorption of dietary copper and its hepatic excretion in bile. In Wilson's disease, hepatic copper is neither excreted in bile, nor incorporated into ceruloplasmin. This abnormality causes the accumulation of copper to toxic levels and its storage mainly in liver, brain, and cornea. The signs of Wilson’s disease are associated with liver diseases and neurological symptoms. The diagnosis is based on the elevated urinary and hepatic copper and low ceruloplasmin levels. Management of Wilson's disease involves decreasing the excess levels of copper, chelation therapy, and oral zinc therapy. In some cases, liver transplantation may be necessary [46].

In this work, a series of silica-coated superparamagnetic $Fe_3O_4@SiO_2$ core-shell nanoparticles with modified surfaces differing in the number of amino groups in outer chains — $Fe_3O_4@SiO_2$-N_1, $Fe_3O_4@SiO_2$-N_2, $Fe_3O_4@SiO_2$-N_3 — (see, Figure 1) was synthesised. The characterisation of the obtained structures was performed using SEM, TEM, FT-IR, and XPS method. Subsequently, the capability of functionalised nanoparticles concerning simultaneous Cd^{2+}, Pb^{2+}, and Cu^{2+} ion binding was studied using electrochemical techniques, such as DPV in combination with HMDE and preconcentration method. Finally, the adsorption-desorption experiments using DPASV method were performed for the first time to examine the Cu^{2+} binding by $Fe_3O_4@SiO_2$-N_3 nanoparticles in an aqueous solution.

2. Experimental

2.1. Reagents

All reagents, analytical grade, were purchased from the indicated suppliers and used without further purification. Aqueous solutions were prepared using ultra-pure deionised water. Ferric chloride hexahydrate ($FeCl_3 \cdot 6H_2O$) and ferrous chloride tetrahydrate ($FeCl_2 \cdot 4H_2O$), ammonia (25%), tetraethyl orthosilicate (98 %) (TEOS), 3-(aminopropyl)triethoxysilane (APTES) (99 %), N-(2-aminoethyl)-3-aminopropyltrimethoxysilane and N^1-(3-trimethoxysilylpropyl)diethylenetriamine were purchased from Sigma-Aldrich (Poland). The organic solvents, potassium chloride KCl (99.9 %), cadmium nitrate tetrahydrate $Cd(NO_3)_2 \cdot 4H_2O$ (99.9 %), lead nitrate $Pb(NO_3)_2$, and copper nitrate trihydrate $Cu(NO_3)_2 \cdot 3H_2O$ (99.9 %) were purchased from POCh (Poland).

2.2. Synthesis of Fe_3O_4

Fe_3O_4 nanoparticles were obtained by the coprecipitation method in an aqueous solution according to the procedure described by Panta et al. [47]. The reaction was performed in non-oxidising conditions maintaining the precise 1 to 2 molar ratio of Fe^{2+}/ Fe^{3+} in an alkaline solution. The advantages and disadvantages of the synthesis reducing conditions were previously described by Kim [48]. The Fe_3O_4 nanoparticles were obtained by dissolving 10.81 g (0.04 mol) of $FeCl_3 \cdot 6H_2O$ and 3.98 g (0.02 mol) of $FeCl_2 \cdot 4H_2O$ in 50 mL of deionised water. Next, argon was passed through the vigorously stirred solution to eliminate oxygen and then the reaction mixture was heated to 70 °C. When the set temperature was reached, 500 mL of ammonium hydroxide solution was added dropwise up to pH 11, what resulted in the formation of Fe_3O_4. Obtained nanoparticles were washed with water to neutralise pH, washed with methanol, and dried.

2.3. Synthesis of core-shell $Fe_3O_4@SiO_2$ nanoparticles

Synthesis of $Fe_3O_4@SiO_2$ was conducted according to Ströber procedure, which mechanism and optimisation were widely described in the literature [47,49–52]. 0.1 g of Fe_3O_4 nanoparticles was dispersed in the mixture of ethanol and water (60:10, v/v) using an ultrasonic bath for 15 min. Subsequently, 1 mL of ammonium hydroxide and 2 mL of tetraethyl orthosilicate (TEOS) were added dropwise to the stirring solution at room temperature. After 24 h, the obtained nanoparticles were washed with water and ethanol and dried in vacuum at 60 °C.

2.4. Modification of core-shell Fe_3O_4@SiO_2 nanoparticles by amine derivatives

The functionalisation of Fe_3O_4@SiO_2 nanoparticles by amine derivatives was performed in anhydrous toluene [53–55] to achieve optimal surface coverage. 4 mL of 3-amino propyl-triethoxysilane (APTES), N-(2-aminoethyl)-3-aminopropyl trimethoxysilane, or *N*^{1}-(3-trimethoxysilylpropyl diethylenetriamine was added to 0.5 g of Fe_3O_4@SiO_2 nanoparticles dispersed in 100 mL of anhydrous toluene using ultrasonic bath. Then, the mixture was mechanically stirred for 12 h at 90 °C. After cooling to room temperature, the obtained Fe_3O_4@SiO_2-N_n amino derivatives (Fe_3O_4@SiO_2-N_1, Fe_3O_4@SiO_2-N_2, or Fe_3O_4@SiO_2-N_3) were magnetically collected, washed several times using absolute ethanol, and dried under vacuum at 50 °C (Figure 1).

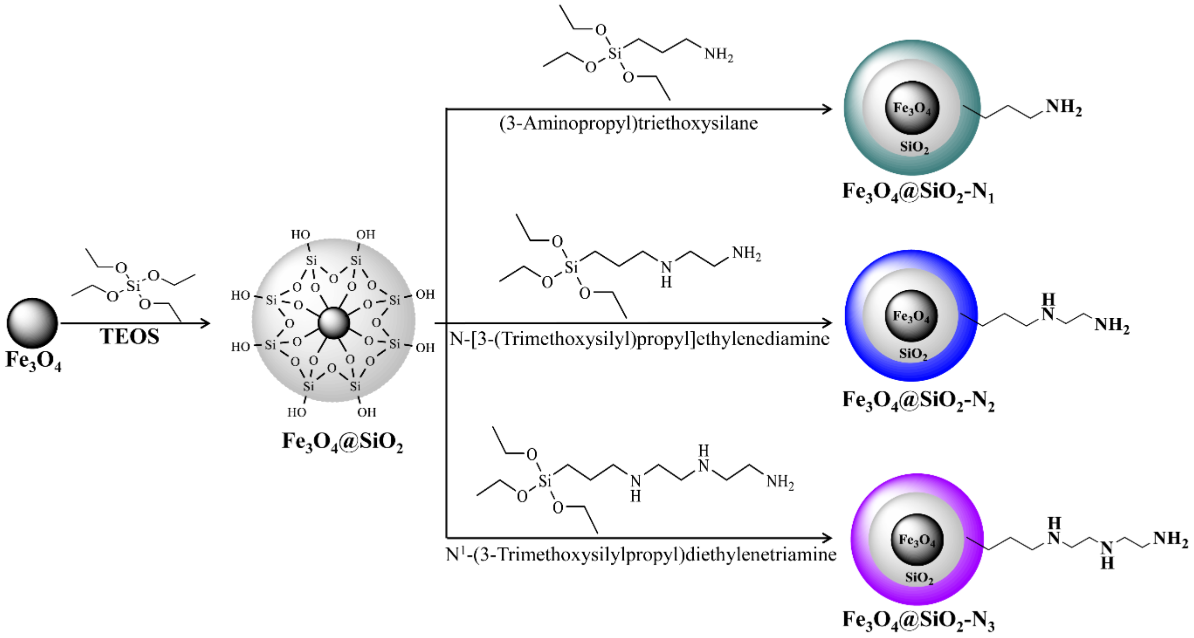

Figure 1. Scheme of Fe_3O_4@SiO_2-N_n nanoparticles synthesis.

2.5. Methods

The images of all $Fe_3O_4@SiO_2\text{-}N_n$ nanoparticles were obtained using the scanning electron microscope (SEM) — JEOL JSM7001F, operating at 9.5 kV — and transmission electron microscopy (TEM) — Tecnai G2 Spirit BioTWIN FEI, operating at 120 kV. All nanoparticles samples for TEM imagining were sonicated for 30 min in the absolute ethanol solution.

Fourier Transform Infrared Spectroscopy (FT-IR) spectra were obtained with the KBr pellet method using Bruker FRA 106 spectrometer.

X-Ray Photoelectron Spectroscopy (XPS) was utilised to evaluate the chemical composition of the investigated nanoparticles. For this purpose, the high-resolution scans were performed in Fe2p, C1s, O1s, N1s, and Si2p binding energy range. The measurements were carried out on Escalab 250Xi spectroscope, ThermoFisher Scientific. The monochromatic AlKα excitation source was used with a spot diameter of 250 µm. 10 eV pass energy and 0.05 eV energy step size were utilised. The charge compensation was achieved through the low-energy electron and low-energy Ar^+ ions flow, with the final calibration of the XPS spectra for peak characteristics adventitious carbon C1s at 284.7 eV. The peak deconvolution was carried out using Avantage software provided by the spectroscope manufacturer.

All electrochemical measurements were carried out using Mercury Electrode Metrohm 663 VA Stand integrated with Autolab potentiostat/galvanostat PGSTAT-128N controlled with NOVA 2.1.4 software. The three-electrode cell contained Static Drop Mercury Electrode (SDME) as a working electrode. Calomel $Hg|Hg_2Cl_2|KCl_{(saturated)}$ and glassy carbon (GC) were used as the reference and counter electrode, respectively.

Differential pulse voltammetry (DPV) was utilised for the detection of Cd^{2+}, Pb^{2+}, and Cd^{2+} ions under optimised experimental conditions: deposition potential -0.9 V, deposition time 90 s, modulation amplitude 0.05 V, modulation time 0.07 s, interval time 1.85 s, and step potential 0.005 V. All measurements were conducted in Teflon cell to avoid a sorption of metal ions on the glass surface.

The ion detection was performed in a potential range of -0.8 V to 0.0 V. The solutions of metal ions were prepared using potassium chloride KCl, pH 6.5 as the supporting electrolyte. $Fe_3O_4@SiO_2\text{-}N_n$ nanoparticles were prepared by dispersion using the ultrasonic bath for 30 min before each measurement.

2.6. Determination of removal efficiency

The adsorption-desorption experiment was conducted to examine the efficiency of Cu^{2+} removal from an aqueous solution. The ion desorption process was investigated in 0.1 M HCl solution which was used as a desorbing agent. 5.08 mg of $Fe_3O_4@SiO_2-N_3$ was used to capture copper ions present in 10 mL of 4.3 μM Cu^{2+} solution. The solution was then left for 40 min at room temperature with shaking. Subsequently, all nanoparticles were collected magnetically and the supernatant was removed. Then, 10 mL of 0.1 M HCl was added to $Fe_3O_4@SiO_2-N_3$ nanoparticles with adsorbed Cu^{2+} and mixed with a stream of argon. The measurement of desorbed Cu^{2+} concertation was performed immediately using DPASV technique. The removal efficiency was calculated by the determination of the obtained voltammograms peak area for the standard solution and after desorption in 0.1 M HCl.

3. Results and discussion

3.1. SEM and TEM — Morphology analysis

In the first step, the obtained $Fe_3O_4@SiO_2$-N_n nanoparticles were characterised using Scanning Electron Microscopy and Transmission Electron Microscopy (Figure 2). SEM and TEM images of magnetite nanoparticles modified with different length of amino chains showed that the nanostructures received by co-precipitation method are highly homogeneous in shape and size. Figure 3 confirms the presence of small and quasi-spherical core-shell structures. The average size of all $Fe_3O_4@SiO_2$-N_n nanoparticles was approximately 30 – 50 nm. All of the examined nanoparticles were in the agglomerated state due to their natural tendency to form agglomerates based on their magnetic nature.

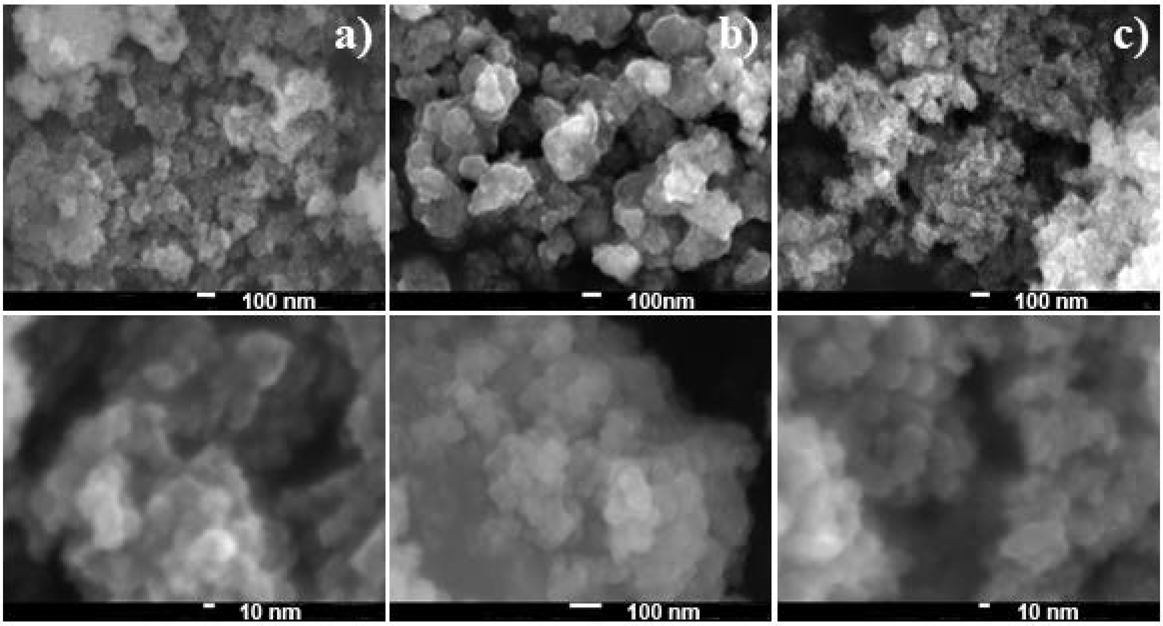

Figure 2. SEM images of: column a) $Fe_3O_4@SiO_2$-N_1, column b) $Fe_3O_4@SiO_2$-N_2, and column c) $Fe_3O_4@SiO_2$-N_3.

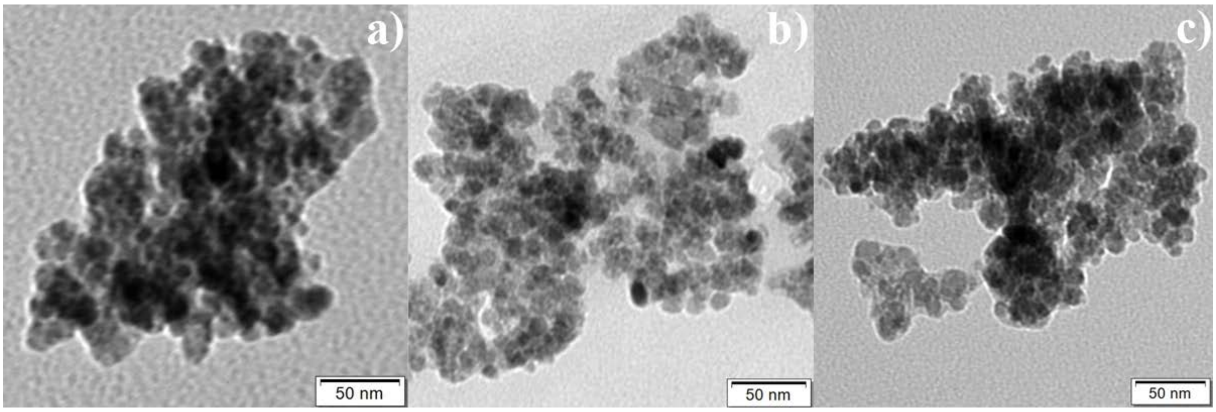

Figure 3. TEM images of: a) $Fe_3O_4@SiO_2$-N_1, b) $Fe_3O_4@SiO_2$-N_2, and c) $Fe_3O_4@SiO_2$-N_3.

3.2. FT-IR spectroscopy analysis

The FT-IR spectra were obtained to compare the spectroscopic differences and to validate the presence of functional groups on the nanomagnetite surface. Figure 4 a) shows the FT-IR spectra for pure Fe_3O_4 nanoparticles and silica-coated $Fe_3O_4@SiO_2$ as a reference and for nanoparticles functionalised by amino groups $Fe_3O_4@SiO_2$-N_1, $Fe_3O_4@SiO_2$-N_2, and $Fe_3O_4@SiO_2$-N_3. For all samples, two characteristic bands were shown at wavenumbers 453 cm^{-1} and 597 cm^{-1} from metal-oxygen stretching at Fe^{3+} site [56–58]. In all IR spectra, the decrease in the intensity of the Fe-O band for nanoparticles coated with silica and amino groups was observed. The decrease in the band intensity confirms that the nanoparticles surface was successfully functionalised [59]. Spectra for silica-coated nanoparticles showed a broad, strong band near 1096 cm^{-1} region assigned to symmetric and asymmetric Si-O-Si stretching vibrations caused by the coating of silica shells on the magnetite surface [60].

On the spectra of all amino-modified nanoparticles (Figure 4 b) a new band appeared in the region of 1563 cm^{-1} and 3402 cm^{-1} attributed to N-H stretching vibrations of amino groups. These bands confirm the successful amino-functionalisation of the silica layer on $Fe_3O_4@SiO_2$ nanoparticles and the presence of terminal $–NH_2$ [61,62].

Additionally, a weak band at 1458 cm^{-1} attributed to the C-N stretch vibration was noticed [63]. The absorption bands at about 2930 cm^{-1} and 2850 cm^{-1} are the result of C-H stretching vibrations in the carbon chain [64].

These FT-IR spectra confirmed the formation of a silica shell on the surface of Fe_3O_4 and the amino-functionalisation of the $Fe_3O_4@SiO_2$ core-shell nanostructures.

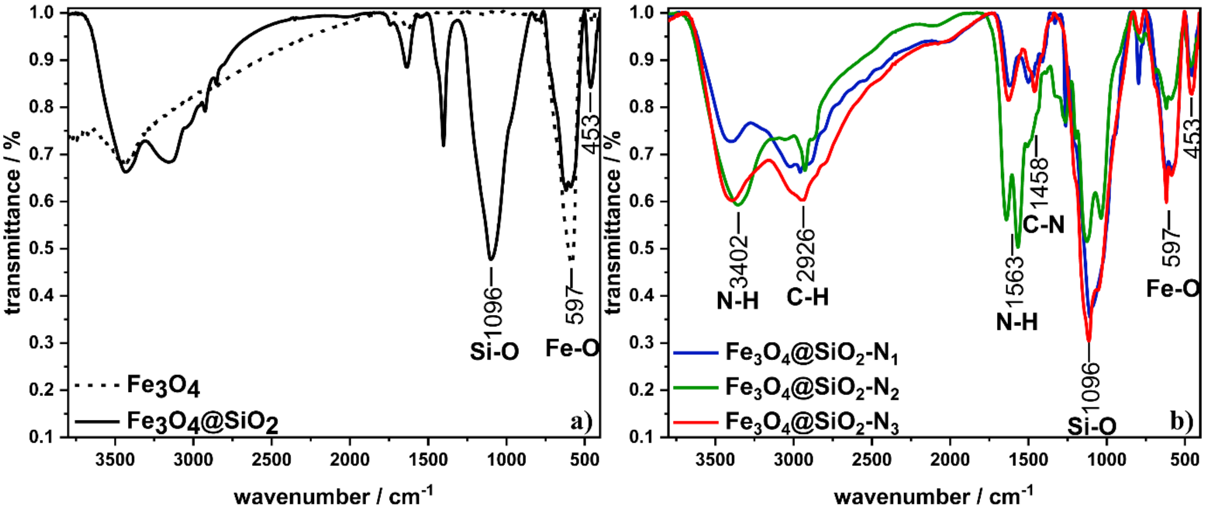

Figure 4. FT-IR spectra for non-functionalised a) Fe_3O_4, $Fe_3O_4@SiO_2$ and b) functionalised $Fe_3O_4@SiO_2$-N_1, $Fe_3O_4@SiO_2$-N_2, and $Fe_3O_4@SiO_2$-N_3 nanoparticles.

3.3. XPS analysis

Moreover, we performed the XPS analyses for all obtained samples to confirm the structure of formed core-shell nanoparticles. The results of the high-resolution XPS analysis are collectively presented in Figure 5 and Table 1 for each of the analysed samples.

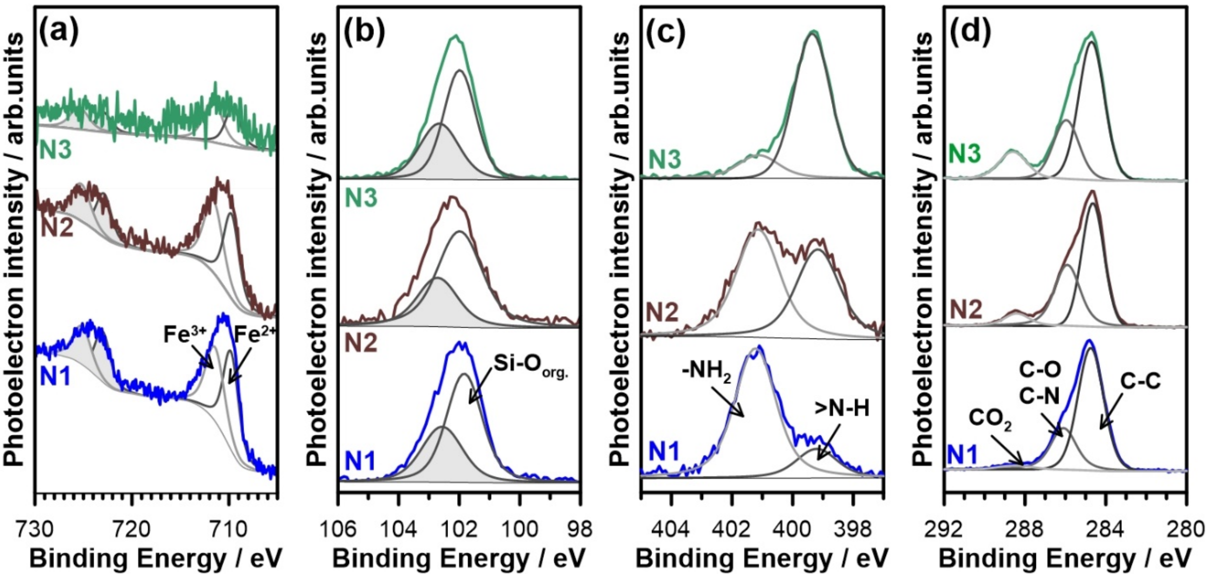

Figure 5. High-resolution XPS spectra obtained for each investigated nanoparticle $Fe_3O_4@SiO_2-N_1$, $Fe_3O_4@SiO_2-N_2$, and $Fe_3O_4@SiO_2-N_3$ within the analysed binding energy range: (a) *Fe2p*, (b) *Si2p*, (c) *N1s*, and (d) *C1s* with superimposed deconvolution according to the model described below. The grey areas represent the $Fe2p_{1/2}$ and $Si2p_{1/2}$ peaks in *Fe2p* and *Si2p* peak doublets, respectively.

The deconvolution in *Fe2p* binding energy (BE) range can be carried out with two spin-orbit doublets, characteristic for both Fe^{2+} and Fe^{3+}. Furthermore, *Fe2p* signal for $Fe_3O_4@SiO_2-N_3$ was barely detected [65–67]. The peak position remains unaltered for each studied compound, proving that modification of the organic chain does not influence the inner shell structure. Similar to the case of Fe_3O_4, the amount of silica is at its peak for $Fe_3O_4@SiO_2-N_1$ functionalisation. Moreover, the significant differences were not observed between $Fe_3O_4@SiO_2-N_2$ and $Fe_3O_4@SiO_2-N_3$ samples in this case, what may imply that the thickness of the organic amino shell is similar for both of these nanoparticles.

The shape of recorded *N1s* spectra reveal major differences between the analysed samples. Each of the nanoparticles contains nitrogen in two different chemical states, while their quantity differs significantly. Two deconvolution spectra used in the proposed model peak at 399.2 and 401.2 eV. The peak at higher BE’s, dominant in the case of $Fe_3O_4@SiO_2-N_1$ sample, should represent the terminal amino-NH_2 functional groups in the compound. The presence of >N-H tertiary amino groups in Fe_3O_4@SiO_2-N_2 and Fe_3O_4@SiO_2-N_3 nanoparticles is reflected in *N1s* spectra with the increasing contribution of the component, located at lower binding energy range. Here, the share of terminal amino groups is reduced to 45 % for Fe_3O_4@SiO_2-N_2 and to 18 % for Fe_3O_4@SiO_2-N_3 samples. The aforementioned model finds a good correlation with the literature findings. The presence of N-H groups in Fe_3O_4@SiO_2-N_1 can be associated with the adsorption of CO_2 from the ambient atmosphere [68–70].

The presence of Si-O bonds with the organic chain was confirmed by a strong peak doublet at 101.7 eV. Similar values were previously reported for silicone groups in silanes and other organic, silicon-containing compounds [58,71]. Finally, the *C1s* peak region was analysed and deconvoluted in three different chemical states. The most significant component, detected at 284.7 eV, should be ascribed to C-C and C-H bonds in the functionalisation molecules forming the shell of the nanoparticles. Its total share in the analysed signal ranges between 33.3 and 36.8 at.%. Importantly, the presence of the component mentioned above may be caused by adventitious carbon from the air exposure [72]. The second notable component lies at 286.2 eV, an energy range typical for C-N bonds in amines and C-O bonds [73,74]. The share of the organic chain (measured as a sum of C-C and C-N components) is naturally the most prominent for the shortest amino chains with Fe_3O_4@SiO_2-N_1 molecule functionalisation. However, the significant differences were not observed between Fe_3O_4@SiO_2-N_2 and Fe_3O_4@SiO_2-N_3 samples, what is similar to the earlier conclusion regarding *Si2p* component. Finally, the last *C1s* peak emerges for both Fe_3O_4@SiO_2-N_2 and Fe_3O_4@SiO_2-N_3 samples, at energies exceeding 288 eV. This component is most often ascribed to carbon dioxide, which is probably adsorbed onto the nanoparticles surface [75]. Surface defects as well as structure modifications of the examined compounds influence the CO_2 adsorption [76,77]. Since its contribution is the highest for the Fe_3O_4@SiO_2-N_3 sample, it is suggested that its presence is connected with changes within >NH groups.

These analyses are confirmed in the distribution of various components in *O1s* spectra, which were deconvoluted in three peaks, connected with iron oxides (529.9 eV), silica, and possible C-O interaction (531.7 eV) and C=O bonds (533.5 eV). The Fe_3O_4 signal is the strongest for Fe_3O_4@SiO_2-N_1 sample and is up to four times weaker for Fe_3O_4@SiO_2-N_3, where, on the other hand, the signal from C=O bonds is more prominent. The two times higher contribution from silica in the *O1s* of Fe_3O_4@SiO_2-N_1 sample was also confirmed, strongly supporting the hypothesis regarding the smaller functionalisation thickness of these nanoparticles.

Table 1. Surface chemical composition of $Fe_3O_4@SiO_2$-N_1, $Fe_3O_4@SiO_2$-N_2, and $Fe_3O_4@SiO_2$-N_3 samples based on the deconvoluted high-resolution XPS spectra.

	Fe2p		*Si2p*	*N1s*		*C1s*			*O1s*		
	Fe^{2+}	Fe^{3+}	Si-O	>NH	-NH_2	C-C	CN	C=O	Fe-O	Si-O	C=O
BE / eV	709.8	711.4	101.7	399.2	401.2	284.7	286.1	288.5	529.9	531.7	533.5
N_1	1.1	1.0	13.0	1.3	5.7	33.3	12.8	1.3	4.0	25.3	1.2
N_2	0.7	0.7	7.9	2.8	3.4	34.2	22.0	4.4	2.6	16.9	4.3
N_3	0.1	0.1	7.9	8.2	1.7	36.8	16.1	8.0	0.9	17.0	3.1

3.4. Simultaneous electrochemical determination of Cd^{2+}, Pb^{2+}, and Cu^{2+}

The individual and simultaneous determination of Cd^{2+}, Cu^{2+}, and Pb^{2+} applying amino-functionalised Fe_3O_4@Carbon microspheres were previously measured by Bai et al. [78] using modified glassy carbon electrode.

In this work, the simultaneous detection of Cd^{2+}, Pb^{2+}, and Cu^{2+} was carried out under optimised experimental conditions using DPASV technique and HDM electrode. The main advantage of these electrodes, besides its surface reproducibility and fast measurement, [79] is the analysis of Fe_3O_4@SiO_2-N_n nanoparticles to assess their capability for binding the metal ions without electrode modification. We investigated three types of nanoparticles differing in the number of amino groups in the outer carbon chain — Fe_3O_4@SiO_2-N_1 with one amino group, Fe_3O_4@SiO_2-N_2 with two amino groups, and Fe_3O_4@SiO_2-N_3 with three amino groups.

To achieve this goal, all measurements were conducted under laboratory conditions to reduce the risk of environmental mercury contamination. Mercury from HDME can be reused after proper treatment. Two-stage DPASV analysis involved pre-concentration and metal ions stripping. First, the Cd^{2+}, Pb^{2+}, and Cu^{2+} ions were electrodeposited onto the working electrode by application of the negative potential (-0.9 V). Subsequently, the faradic current obtained by oxidation was recorded during the potential sweep toward the anodic direction (-0.8 V to 0.0 V).

To examine the selected ion binding abilities of Fe_3O_4@SiO_2-N_1, Fe_3O_4@SiO_2-N_2, and Fe_3O_4@SiO_2-N_3, series of measurements were performed in the solution containing Cd^{2+}, Pb^{2+}, and Cu^{2+}, 4.5 µM concentration. All electrochemical experiments were performed in 0.5 M KCl pH = 6.5 due to the formation of hydroxides of utilised metals at pH higher than 7 [58]. Furthermore, the adsorption of metal ions depends on the charge located on the nanocomposite surface and the number of functional groups [80].

Three well-defined peaks at -0.63 V, -0.42 V, and -0.17 V in anodic stripping voltammograms confirm the presence of Cd^{2+}, Pb^{2+}, and Cu^{2+} in the solution, respectively (see, Figure 6). During the next portions of nanoparticles addition, a decrease in the intensity of the ions peaks was observed. The rate of peaks intensity change depended on the determined ion and used nanoparticles type. In all presented voltammograms, the dilution factor was expressed by the formula: $DF = \frac{V_0 + V_S}{V_0}$, where V_0 is the initial volume and V_s is the step volume applied.

Figure 6 a) presents the voltammograms obtained during the titration of Cd^{2+}, Pb^{2+}, and Cu^{2+} by Fe_3O_4@SiO_2-N_1. The metal ion peaks intensity decreased during the addition of the next portions of nanoparticles in an amount of 1.18 mg to 9.41 mg, conducted in eight steps.

The obtained results directly indicate that the initial linear current peak (blue intermittent line) decreases for Pb^{2+} and Cu^{2+} ions of each nanoparticles portion.

The intensity of Cd^{2+} peak decreased by a half and remained at this stable level. After the addition of 7.06 mg of nanoparticles, the equilibrium was established and the next portion of nanoparticles caused no changes in the current peak intensity. The $Fe_3O_4@SiO_2$-N_1 binding percentage was calculated (Figure 6 b) for Pb^{2+} and Cu^{2+} and reached 99.7 % and 92.8 %, respectively. However, the binding percentage for Cd^{2+} remained stable at the level of 40 %. These results indicate that $Fe_3O_4@SiO_2$-N_1 nanoparticles express high sensitivity towards Pb^{2+} and Cu^{2+}, what is observed by binding of these ions in nearly 100 %.

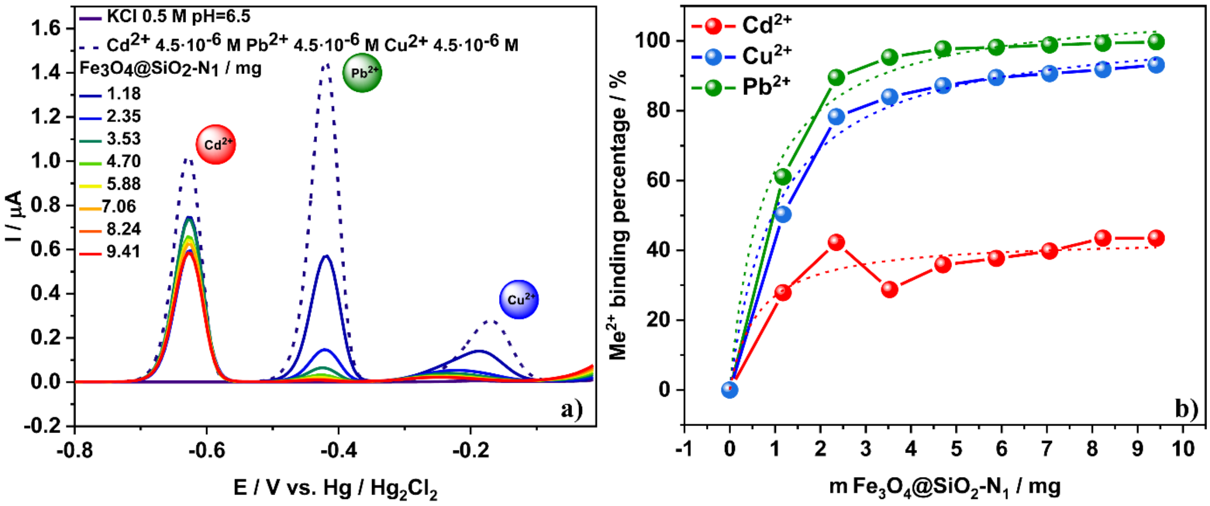

Figure 6. a) Anodic stripping voltammograms and b) percentage of Cd^{2+} (4.5 µM), Pb^{2+} (4.5 µM) and Cu^{2+} (4.5 µM) binding by $Fe_3O_4@SiO_2$-N_1 nanoparticles.

In the next step, we conducted the simultaneous experiments using Cd^{2+}, Pb^{2+} and Cu^{2+} to evaluate the $Fe_3O_4@SiO_2$-N_2 nanoparticles binding capacity. The titration of Cd^{2+}, Pb^{2+}, and Cu^{2+} was carried out in five steps using various amounts of $Fe_3O_4@SiO_2$-N_2 nanoparticles — 0.83 mg to 8.27 mg (Figure 7a).

Surprisingly, besides a decrease in the peak intensity observed during Cd^{2+}, Pb^{2+} titration, we also detected a slight shift in the peaks towards lower potentials. Figure 7a shows the voltammograms where a complete disappearance of Pb^{2+} peak and decrease in the Cd^{2+} peak intensity were observed.

In the case of Cu^{2+} titration (Figure 7a), the effect of the signal decreasing is observed only in the first two steps, following a comparable signal level afterwards, shifted toward negative potentials. This phenomenon is probably associated with the adsorption of nanoparticles and their complexes to the mercury drop [81]. The irregular changes in the peak intensity clearly indicate that the equilibrium is not establishing.

After addition of 3.31 mg $Fe_3O_4@SiO_2$-N_2 no significant changes in the voltammogram were observed. Figure 7b shows the binding percentage for $Fe_3O_4@SiO_2$-N_2 nanoparticles. The percentage of Pb^{2+} and Cd^{2+} ion binding by $Fe_3O_4@SiO_2$-N_2 was established at 98.5 % and 66.6%, respectively. It is worth to notice that there was no ion binding observed for Cu^{2+}. The percentage of Cu^{2+} binding by $Fe_3O_4@SiO_2$-N_2 remains at 0 % even if nanoparticles were added in an excess. An average of obtained results and slight differences in Cu^{2+} peak intensity were regarded as measurement errors.

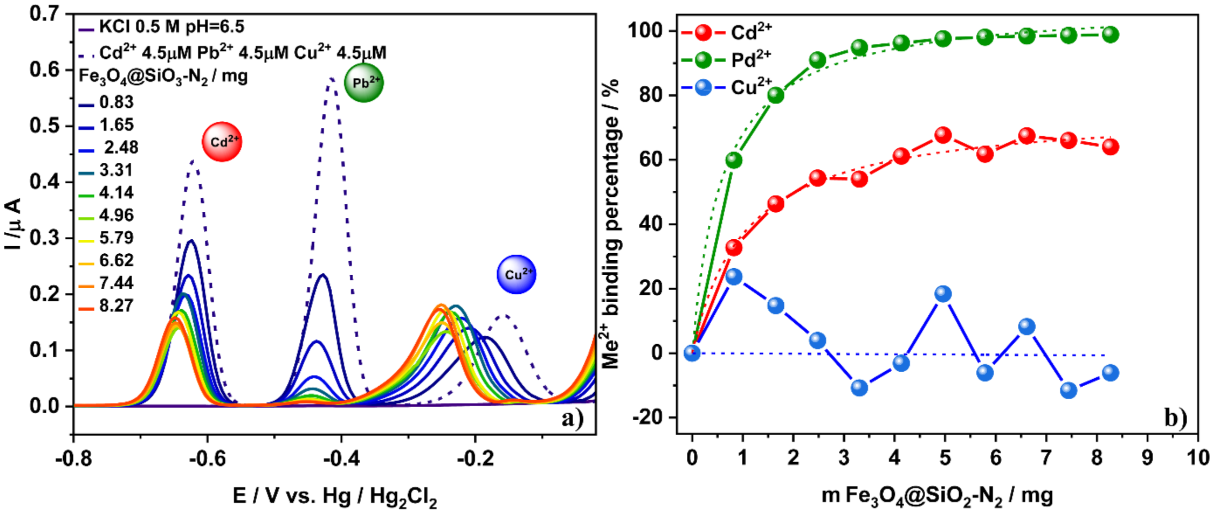

Figure 7. a) Anodic stripping voltammograms and b) percentage of Cd^{2+} (4.5 μM), Pb^{2+} (4.5 μM), and Cu^{2+} (4.5 μM) binding by $Fe_3O_4@SiO_2$-N_2 nanoparticles.

The voltammograms presented in Figure 8a reveal the Cd^{2+}, Pb^{2+}, and Cu^{2+} titration by $Fe_3O_4@SiO_2$-N_3 in twelve steps in the nanoparticles amount range of 0.05 mg to 3.97 mg. The addition of the next nanoparticles portions led only to the disappearance of the Cu^{2+} peak. The Cd^{2+} and Pb^{2+} slight peak intensity changes were considered to be in the range of measurement error. For $Fe_3O_4@SiO_2$-N_3 nanoparticles, the Cu^{2+} binding percentage reached 92.5 %, while 0 % binding percentage was observed for Cd^{2+} and Pb^{2+} ions (Figure 8 b).

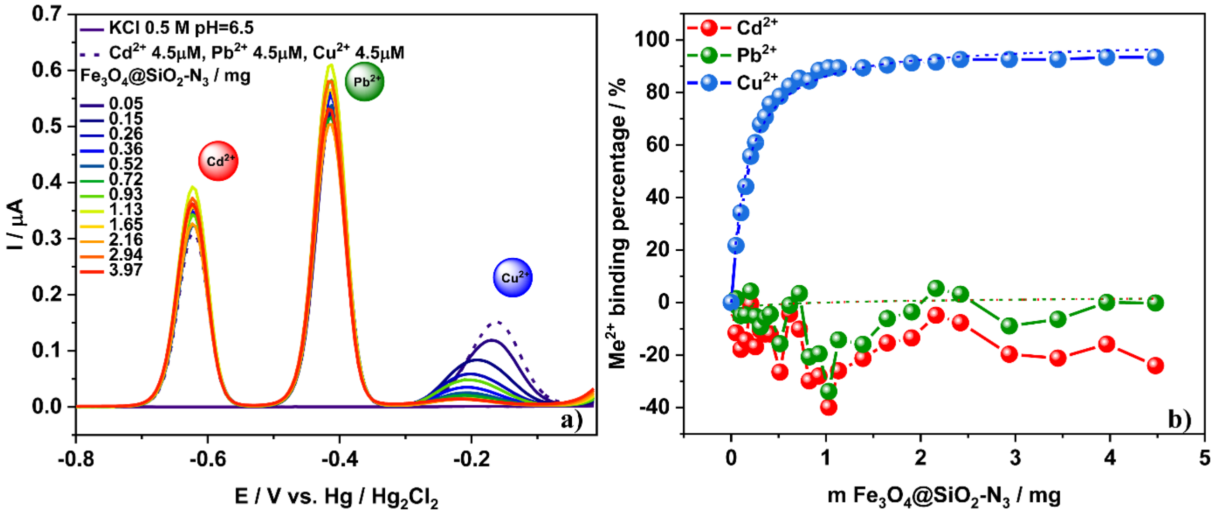

Figure 8. a) Anodic stripping voltammograms and b) percentage of Cd^{2+} (4.5 µM), Pb^{2+} (4.5 µM), and Cu^{2+} (4.5 µM) binding by $Fe_3O_4@SiO_2\text{-}N_3$ nanoparticles.

Figure 9 presents the comparison of ion binding percentage for each $Fe_3O_4@SiO_2\text{-}N_n$ nanoparticle. The binding percentage was recounted for 4 mg of nanoparticles added to the ion solution. The highest observed binding percentage for Pb^{2+} was over 96%, both for $Fe_3O_4@SiO_2\text{-}N_1$ and $Fe_3O_4@SiO_2\text{-}N_2$. The slightly smaller binding percentage was observed for Cu^{2+} binding by $Fe_3O_4@SiO_2\text{-}N_3$ and $Fe_3O_4@SiO_2\text{-}N_1$ resulting in 93.4 % and 85.5 %, respectively.

Furthermore, there was no Cd^{2+}, Pb^{2+}, and Cu^{2+} binding observed for $Fe_3O_4@SiO_2\text{-}N_3$, $Fe_3O_4@SiO_2\text{-}N_3$, and $Fe_3O_4@SiO_2\text{-}N_2$, respectively. These results directly indicate that the $Fe_3O_4@SiO_2\text{-}N_3$ nanoparticles bind Cu^{2+} with high selectivity.

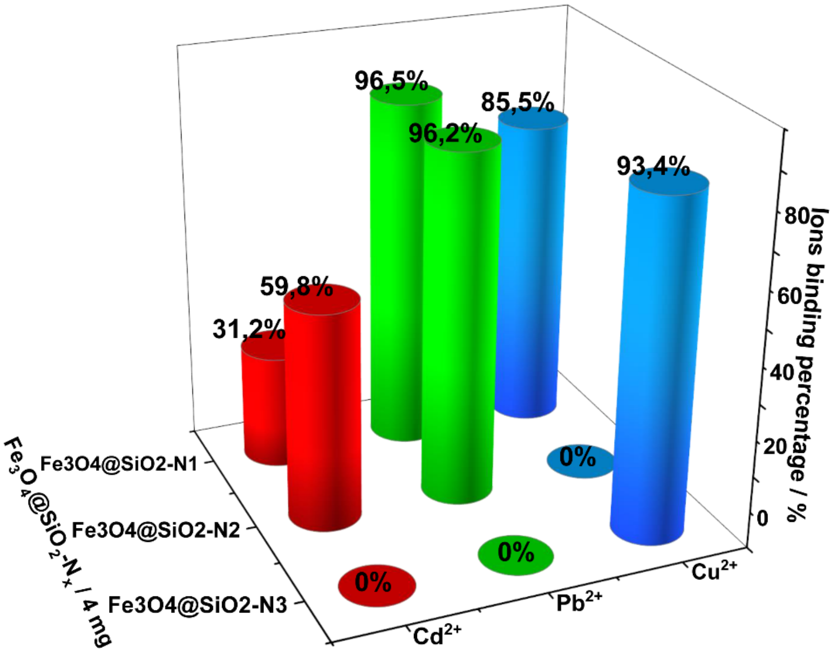

Figure 9. Cd^{2+}, Pb^{2+}, Cu^{2+} ions binding percentage for $Fe_3O_4@SiO_2$-N_1, $Fe_3O_4@SiO_2$-N_2 and $Fe_3O_4@SiO_2$-N_3 nanoparticles

On the basis of the structural characteristics of Cu (II) diamine complexes supported on silica gel and the distribution of these forms as a function of the pH solution described by Nowicki [82], the proposed structure of copper complex formation by $Fe_3O_4@SiO_2$-N_n is presented in Figure 10. It seems that formation of complexes with metal ions with 1:1 and 1:2 stoichiometry is the key factor in the complexation of ions by amines in the hybrid material (Figure 10).

The number of donor nitrogen atoms in the structure of the complexes, the size of the ions, the density of the charge of metal ions, and the number of water molecules that hydrate both the complexes and ligands significantly determine the stoichiometry and the process of complex formation by the hybrid material [83].

The differences in the binding selectivity for the examined metal ions by $Fe_3O_4@SiO_2$-N_n is probably related to the presence of intramolecular hydrogen bonds occurring both in the external and internal parts of the functional layer. The observation that $Fe_3O_4@SiO_2$-N_1 binds Cd^{2+}, Pb^{2+}, Cu^{2+}, $Fe_3O_4@SiO_2$-N_2 binds Cd^{2+}, Pb^{2+}, and $Fe_3O_4@SiO_2$-N_3 binds only Cu^{2+} results from these interactions. The aqua and amino complexes form between metal ions and amines with the deposition directly on a hybrid material. Subsequently, free electron pairs in this material, which come to varying degrees from nitrogen atoms of amines, determine the manner and selectivity of the ion binding with the studied material.

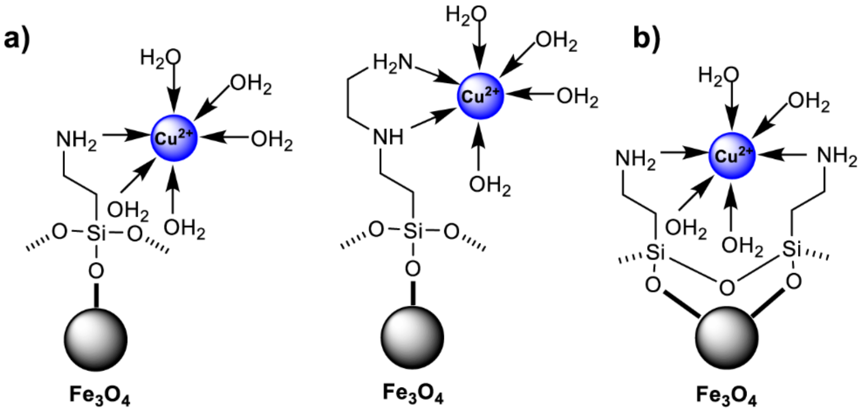

Figure 10. Proposed structure of the two-type complexes a) 1:1 and b) 1:2 $Fe_3O_4@SiO_2\text{-}N_n$ nanoparticles and ion metal interactions.

3.5. Cu^{2+} adsorption-desorption experiment using $Fe_3O_4@SiO_2$-N_3 nanoparticles

Based on the high selectivity of $Fe_3O_4@SiO_2$-N_3 for Cu^{2+} which was observed using electrochemical method, we decided to evaluate the adsorption-desorption properties only of this studied nanoparticle. It is worth to notice that, according to the authors' knowledge, this experiment using DPASV was performed for the first time. The procedure of Cu^{2+} adsorption was described in the experimental section. 5.08 mg of $Fe_3O_4@SiO_2$-N_3 was used to bind 43 nmol of Cu^{2+} in 0.5 M KCl solution. The adsorption process for nanoparticles containing an amino group is usually performed from a couple of minutes to hours [84–86,43]. In this work, the adsorption process was performed within 40 min incubation time at room temperature, with shaking. The desorption process was performed in 0.1 M HCl to obtain acidic pH and protonation of amino groups leading to the Cu^{2+} ions desorption. The desorption process was conducted using DPASV method directly after the addition of HCl. According to the previous research, the hydrochloric acid was selected as an optimal desorption agent [61,84]. In other study the desorption time ranged from 5 min to 40 min [43,85]. We, however, established the desorption time which was shorter than 5 minutes. Figure 11 shows the voltammograms obtained for standard Cu^{2+} solution and after the nanoparticles regeneration. The peak shift is the consequence of different pH of the solution. The calculated Cu^{2+} removal efficiency was 99.9 %.

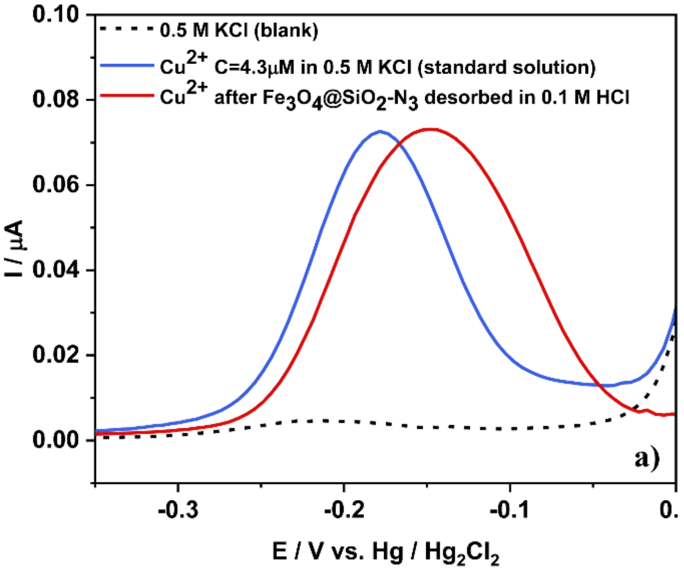

Figure 11. Comparison of anodic stripping voltammograms of 0.5 M KCl electrolyte (blank), Cu^{2+} standard solution C = 4.3 µM, Cu^{2+} after $Fe_3O_4@SiO_2$-N_3 nanoparticles regeneration.

Proper selection of pH range, which effects the behaviour of the nanoparticles, the form of determined metal ion, and its solubility, is the most important factor for the examination of the adsorption and desorption process efficiency [86]. The form of Cu^{2+} depends on the pH value of the solution. Cu^{2+} species occur at pH <7 [84,87]. At pH>7 different derivative products of Cu^{2+} hydrolysis — $Cu_2(OH)_2^{2+}$, $Cu(OH)^+$, $Cu(OH)_2$, $Cu(OH)_3^-$, $Cu(OH)_4^-$ — exist in the solution [88]. The Cu^{2+} quantity drops with the increasing pH value, what leads to the precipitation of various hydrolysis forms of Cu^{2+}. Due to this phenomenon, the adsorption process was performed at pH 6.5.

The adsorption and desorption process occurring for the studied nanoparticles is the consequence of the acid-base interactions. In an aqueous solution both H_3O^+ and metal ions undergo the adsorption processes onto amino groups present in $Fe_3O_4@SiO_2$-N_n nanoparticles (Figure 12). Low pH value causes the increase of H_3O^+ species in a solution and the protonation of amino groups present on the nanoparticles surface. This, in consequence, leads to the decrease in the metal ion concentration due to the nanoparticle adsorption (Figure 12). On the other hand, high pH value is associated with the elevated number of hydroxyl groups in the solution, what causes the amino groups deprotonation (Figure 12). In consequence, the deprotonated amino groups increased the capability of the nanoparticles to bind metal ions [86].

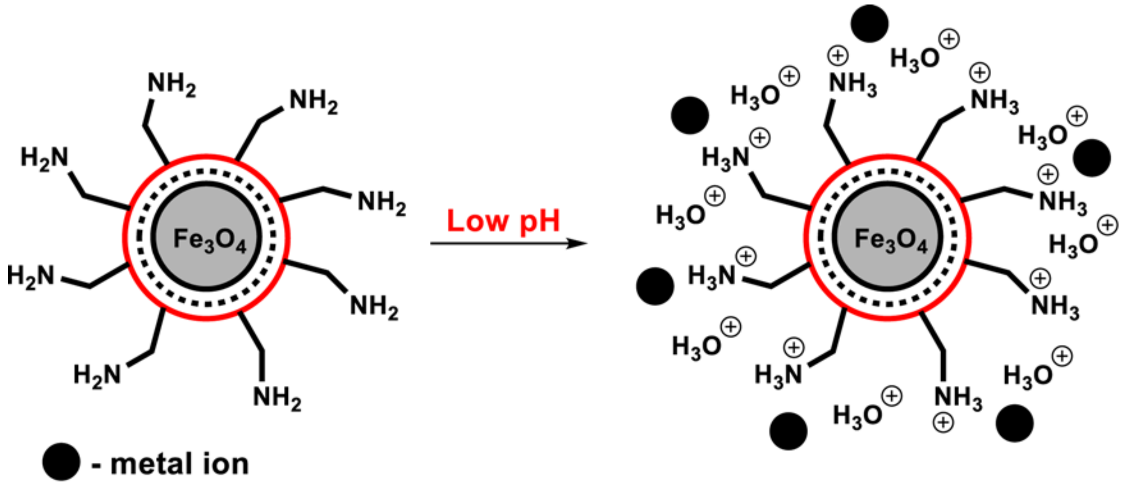

Figure 12. Scheme of the proposed adsorption and desorption mechanism for the $Fe_3O_4@SiO_2$-N_n nanoparticles — metal ions interaction.

4. Conclusions

In present work we examined a series of functionalised magnetite nanoparticles $Fe_3O_4@SiO_2\text{-}N_n$ as a novel Cd^{2+}, Pb^{2+}, Cu^{2+} nano-adsorbent in KCl aqueous solution.

First, we synthetised the nanoparticles coated preliminary with SiO_2 using TEOS and then with various carbon chains containing a different number of amino groups — $Fe_3O_4@SiO_2\text{-}N_1$, $Fe_3O_4@SiO_2\text{-}N_2$, and $Fe_3O_4@SiO_2\text{-}N_3$. FT-IR and XPS spectra confirmed the presence of characteristic functional groups on the nanoparticles surface. Additionally, SEM and TEM analysis were utilised to confirm the homogenous spherical 30 to 50 nm nanostructures.

These three types of obtained nanoparticles were used as Cd^{2+}, Pb^{2+}, Cu^{2+} metal ion adsorbents. Metal ion binding ability of $Fe_3O_4@SiO_2\text{-}N_n$ was measured using DPASV method in combination with HDME in 0.5 M KCl solution.

To compare binding capacity in 4.5 µM Cd^{2+}, Pb^{2+}, and Cu^{2+} solutions, the binding percentage was recalculated for 4 mg of used nanoparticles. Obtained results show that the adsorption rate is different for each ion depending on the nanoparticles type. The ion binding capacity and selectivity depends on the interactions occurring between the outer carbon amino chains and the metal ion.

The highest binding percentage — 96 % — was observed for Pb^{2+} binding for both $Fe_3O_4@SiO_2\text{-}N_1$ and $Fe_3O_4@SiO_2\text{-}N_2$. Furthermore, slightly lower binding level of nearly 93 % was observed for $Fe_3O_4@SiO_2\text{-}N_3$ Cu^{2+}. The middle value of the binding percentage — 85% — was observed for Cu^{2+} binding by $Fe_3O_4@SiO_2\text{-}N_1$. The lowest binding percentage was found in the case of $Fe_3O_4@SiO_2\text{-}N_2$ and $Fe_3O_4@SiO_2\text{-}N_1$ for Cd^{2+} at the level of 60% and 31%, respectively. Moreover, the binding was not observed for Cd^{2+} and Pb^{2+} by $Fe_3O_4@SiO_2\text{-}N_3$ and for Pb^{2+} by $Fe_3O_4@SiO_2\text{-}N_3$. The obtained results show that the nanoparticles with three amino groups in the outer chain — $Fe_3O_4@SiO_2\text{-}N_3$ — bind Cu^{2+} with high selectivity.

Furthermore, we used the adsorption and desorption experiment to analyse the Cu^{2+} binding selectivity of $Fe_3O_4@SiO_2\text{-}N_3$. The obtained results directly indicate that the recovery of Cu^{2+} from the aqueous solution is very high and reached 99.9-%.

Examined series of amino functionalised $Fe_3O_4@SiO_2\text{-}N_n$ nanoparticles are promising metal ion nano-adsorbents due to their high ion capacity, easy separation using magnetic field, and renewability based on the pH value control.

5. Acknowledgements

This study was financed by the University of Gdansk within the project supporting young scientists and PhD students (grant No. BMN 539-8210-B281-18 and 539-8210-B281-19). Authors are grateful to Alexander Company Gdynia for a technical support.

6. References

[1] N.K. Srivastava, C.B. Majumder, Novel biofiltration methods for the treatment of heavy metals from industrial wastewater, Journal of Hazardous Materials. 151 (2008) 1–8. https://doi.org/10.1016/j.jhazmat.2007.09.101.

[2] M. Noreen, M. Shahid, M. Iqbal, J. Nisar, Measurement of cytotoxicity and heavy metal load in drains water receiving textile effluents and drinking water in vicinity of drains, Measurement. 109 (2017) 88–99. https://doi.org/10.1016/j.measurement.2017.05.030.

[3] H.S. Kim, Y.J. Kim, Y.R. Seo, An Overview of Carcinogenic Heavy Metal: Molecular Toxicity Mechanism and Prevention, Journal of Cancer Prevention. 20 (2015) 232–240. https://doi.org/10.15430/JCP.2015.20.4.232.

[4] H. Fu, P. Boffetta, Cancer and occupational exposure to inorganic lead compounds: a meta-analysis of published data., Occupational and Environmental Medicine. 52 (1995) 73–81. https://doi.org/10.1136/oem.52.2.73.

[5] P. Joseph, Mechanisms of cadmium carcinogenesis, Toxicology and Applied Pharmacology. 238 (2009) 272–279. https://doi.org/10.1016/j.taap.2009.01.011.

[6] E.K. Silbergeld, M. Waalkes, J.M. Rice, Lead as a carcinogen: Experimental evidence and mechanisms of action, American Journal of Industrial Medicine. 38 (2000) 316–323. https://doi.org/10.1002/1097-0274(200009)38:3<316::AID-AJIM11>3.0.CO;2-P.

[7] E.K. Silbergeld, Facilitative mechanisms of lead as a carcinogen, Mutation Research/Fundamental and Molecular Mechanisms of Mutagenesis. 533 (2003) 121–133. https://doi.org/10.1016/j.mrfmmm.2003.07.010.

[8] V.N. Bulut, H. Demirci, D. Ozdes, A. Gundogdu, O. Bekircan, M. Soylak, C. Duran, A novel carrier element-free co-precipitation method for separation/preconcentration of lead and cadmium ions from environmental matrices, Environmental Progress & Sustainable Energy. 35 (2016) 1709–1715. https://doi.org/10.1002/ep.12422.

[9] X. Tang, H. Zheng, H. Teng, Y. Sun, J.-S. Guo, W. Xie, Q. Yang, W. Chen, Chemical coagulation process for the removal of heavy metals from water: a review, Desalination and Water Treatment. 57 (2014) 1–16. https://doi.org/10.1080/19443994.2014.977959.

[10] S.E. GHAZY, Separation of Cadmium(II) from Aqueous Solutions by the Precipitate Flotation Technique, Separation Science and Technology. 29 (1994) 935–941. https://doi.org/10.1080/01496399408006637.

[11] M.H. Salmani, M. Davoodi, M.H. Ehrampoush, M.T. Ghaneian, M.H. Fallahzadah, Removal of cadmium (II) from simulated wastewater by ion flotation technique, Iranian J Environ Health Sci Eng. 10 (2013) 16–20. https://doi.org/10.1186/1735-2746-10-16.

[12] J.B. Melville, E. Matijevic, Removal of copper, lead, and cadmium ions by microflotation, Journal of Colloid and Interface Science. 57 (1976) 94–103. https://doi.org/10.1016/0021-9797(76)90179-X.

[13] H. Abu-Qudais, H. Moussa, Removal of Heavy Metals from Wastewater by Membrane Processes: A Comparative Study, Desalination. 164 (2004) 105–110. https://doi.org/10.1016/S0011-9164(04)00169-9.
[14] J. Kheriji, D. Tabassi, B. Hamrouni, Removal of Cd(II) ions from aqueous solution and industrial effluent using reverse osmosis and nanofiltration membranes, Water Sci Technol. 72 (2015) 1206–1216. https://doi.org/10.2166/wst.2015.326.
[15] A.P. de los Ríos, F.J. Hernández-Fernández, L.J. Lozano, S. Sánchez, J.I. Moreno, C. Godínez, Removal of Metal Ions from Aqueous Solutions by Extraction with Ionic Liquids, J. Chem. Eng. Data. 55 (2010) 605–608. https://doi.org/10.1021/je9005008.
[16] G.K. Sarma, S. Sen Gupta, K.G. Bhattacharyya, Nanomaterials as versatile adsorbents for heavy metal ions in water: a review, Environmental Science and Pollution Research. 26 (2019) 6245–6278. https://doi.org/10.1007/s11356-018-04093-y.
[17] S.H. Khorzughy, T. Eslamkish, F.D. Ardejani, M.R. Heydartaemeh, Cadmium removal from aqueous solutions by pumice and nano-pumice, Korean Journal of Chemical Engineering. 32 (2015) 88–96. https://doi.org/10.1007/s11814-014-0168-2.
[18] W.-R. Lim, S.W. Kim, C.-H. Lee, E.-K. Choi, M.H. Oh, S.N. Seo, H.-J. Park, S.-Y. Hamm, Performance of composite mineral adsorbents for removing Cu, Cd, and Pb ions from polluted water, Scientific Reports. 9 (2019) 1–10. https://doi.org/10.1038/s41598-019-49857-9.
[19] R. Wang, R. Liang, T. Dai, J. Chen, X. Shuai, C. Liu, Pectin-based adsorbents for heavy metal ions: A review, Trends in Food Science & Technology. 91 (2019) 319–329. https://doi.org/10.1016/j.tifs.2019.07.033.
[20] J. Li, X. Wang, G. Zhao, C. Chen, Z. Chai, A. Alsaedi, T. Hayat, X. Wang, Metal–organic framework-based materials: superior adsorbents for the capture of toxic and radioactive metal ions, Chemical Society Reviews. 47 (2018) 2322–2356. https://doi.org/10.1039/C7CS00543A.
[21] S. Abdulrazak, K. Hussaini, H.M. Sani, Evaluation of removal efficiency of heavy metals by low-cost activated carbon prepared from African palm fruit, Applied Water Science. 7 (2017) 3151–3155. https://doi.org/10.1007/s13201-016-0460-x.
[22] L. Wang, Y. Wang, F. Ma, V. Tankpa, S. Bai, X. Guo, X. Wang, Mechanisms and reutilization of modified biochar used for removal of heavy metals from wastewater: A review, Science of The Total Environment. 668 (2019) 1298–1309. https://doi.org/10.1016/j.scitotenv.2019.03.011.
[23] S.S. Fiyadh, M.A. AlSaadi, W.Z. Jaafar, M.K. AlOmar, S.S. Fayaed, N.S. Mohd, L.S. Hin, A. El-Shafie, Review on heavy metal adsorption processes by carbon nanotubes, Journal of Cleaner Production. 230 (2019) 783–793. https://doi.org/10.1016/j.jclepro.2019.05.154.
[24] W. Peng, H. Li, Y. Liu, S. Song, A review on heavy metal ions adsorption from water by graphene oxide and its composites, Journal of Molecular Liquids. 230 (2017) 496–504. https://doi.org/10.1016/j.molliq.2017.01.064.
[25] Y. He, P. Wu, W. Xiao, G. Li, J. Yi, Y. He, C. Chen, P. Ding, Y. Duan, Efficient removal of Pb(II) from aqueous solution by a novel ion imprinted magnetic biosorbent: Adsorption kinetics and mechanisms, PLOS ONE. 14 (2019) e0213377 (1-17). https://doi.org/10.1371/journal.pone.0213377.
[26] I. Hasan, R.A. Khan, W. Alharbi, K.H. Alharbi, A. Alsalme, In Situ Copolymerized Polyacrylamide Cellulose Supported Fe3O4 Magnetic Nanocomposites for Adsorptive Removal of Pb(II): Artificial Neural Network Modeling and Experimental Studies, Nanomaterials. 9 (2019) 1687. https://doi.org/10.3390/nano9121687.

[27] V. Nejadshafiee, M.R. Islami, Adsorption capacity of heavy metal ions using sultone-modified magnetic activated carbon as a bio-adsorbent, Materials Science and Engineering: C. 101 (2019) 42–52. https://doi.org/10.1016/j.msec.2019.03.081.

[28] N.T. Abdel-Ghani, G.A. El-Chaghaby, E.-S.A. Rawash, E.C. Lima, Magnetic activated carbon nanocomposite from Nigella sativa L. waste (MNSA) for the removal of Coomassie brilliant blue dye from aqueous solution: Statistical design of experiments for optimization of the adsorption conditions, Journal of Advanced Research. 17 (2019) 55–63. https://doi.org/10.1016/j.jare.2018.12.004.

[29] Y. Ji, C. Ma, J. Li, H. Zhao, Q. Chen, M. Li, H. Liu, A Magnetic Adsorbent for the Removal of Cationic Dyes from Wastewater, Nanomaterials. 8 (2018) 710 (1–13). https://doi.org/10.3390/nano8090710.

[30] C. Jiang, X. Wang, D. Qin, W. Da, B. Hou, C. Hao, J. Wu, Construction of magnetic lignin-based adsorbent and its adsorption properties for dyes, Journal of Hazardous Materials. 369 (2019) 50–61. https://doi.org/10.1016/j.jhazmat.2019.02.021.

[31] E. Ghasemi, A. Heydari, M. Sillanpää, Superparamagnetic Fe3O4@EDTA nanoparticles as an efficient adsorbent for simultaneous removal of Ag(I), Hg(II), Mn(II), Zn(II), Pb(II) and Cd(II) from water and soil environmental samples, Microchemical Journal. 131 (2017) 51–56. https://doi.org/10.1016/j.microc.2016.11.011.

[32] S. Bao, L. Tang, K. Li, P. Ning, J. Peng, H. Guo, T. Zhu, Y. Liu, Highly selective removal of Zn(II) ion from hot-dip galvanizing pickling waste with amino-functionalized Fe 3 O 4 @SiO 2 magnetic nano-adsorbent, Journal of Colloid and Interface Science. 462 (2016) 235–242. https://doi.org/10.1016/j.jcis.2015.10.011.

[33] A. Dolgormaa, C. Lv, Y. Li, J. Yang, J. Yang, P. Chen, H. Wang, J. Huang, Adsorption of Cu(II) and Zn(II) Ions from Aqueous Solution by Gel/PVA-Modified Super-Paramagnetic Iron Oxide Nanoparticles, Molecules. 23 (2018) 2982–2997. https://doi.org/10.3390/molecules23112982.

[34] H. Zheng, L. Zhou, Z. Liu, Z. Le, J. Ouyang, G. Huang, H. Shehzad, Functionalization of mesoporous Fe3O4@SiO2 nanospheres for highly efficient U(VI) adsorption, Microporous and Mesoporous Materials. 279 (2019) 316–322. https://doi.org/10.1016/j.micromeso.2018.12.038.

[35] A. Tadjarodi, A. Abbaszadeh, M. Taghizadeh, N. Shekari, A.A. Asgharinezhad, Solid phase extraction of Cd(II) and Pb(II) ions based on a novel functionalized Fe3O4@ SiO2 core-shell nanoparticles with the aid of multivariate optimization methodology, Materials Science and Engineering: C. 49 (2015) 416–421. https://doi.org/10.1016/j.msec.2015.01.013.

[36] F. Mohammadi, F. Mohammadi, A. Esrafili, H.R. Sobhi, M. Behbahani, M. Kermani, E. Asgari, Z.R. Fasih, Evaluation of adsorption and removal of methylparaben from aqueous solutions using amino-functionalized magnetic nanoparticles as an efficient adsorbent: Optimization and modeling by response surface methodology (RSM), DESALINATION AND WATER TREATMENT. 103 (2018) 248–260. https://doi.org/10.5004/dwt.2018.21781.

[37] A. Sheikhmohammadi, Z. Dahaghin, S.M. Mohseni, M. Sarkhosh, H. Azarpira, Z. Atafar, M. Abtahi, S. Rezaei, M. Sardar, H. Masoudi, M. Faraji, S. Nazari, R.H. Pouya, M. Almasian, The synthesis and application of the SiO 2 @Fe 3 O 4 @MBT nanocomposite as a new magnetic sorbent for the adsorption of arsenate from aqueous solutions: Modeling, optimization, and adsorption studies, Journal of Molecular Liquids. 255 (2018) 313–323. https://doi.org/10.1016/j.molliq.2018.01.164.

[38] A. Sheikhmohammadi, M. Safari, A. Alinejad, A. Esrafili, H. Nourmoradi, E. Asgari, The synthesis and application of the Fe3O4@SiO2 nanoparticles functionalized with 3-aminopropyltriethoxysilane as an efficient sorbent for the adsorption of Ethylparaben

from wastewater: synthesis, kinetic, thermodynamic and equilibrium studies, Journal of Environmental Chemical Engineering. 7 (2019) 103315 (1–9). https://doi.org/10.1016/j.jece.2019.103315.

[39] R. Roto, Y. Yusran, A. Kuncaka, Magnetic adsorbent of Fe 3 O 4 @SiO 2 core-shell nanoparticles modified with thiol group for chloroauric ion adsorption, Applied Surface Science. 377 (2016) 30–36. https://doi.org/10.1016/j.apsusc.2016.03.099.

[40] F. Ghorbani, S. Kamari, Core–shell magnetic nanocomposite of Fe3O4@SiO2@NH2 as an efficient and highly recyclable adsorbent of methyl red dye from aqueous environments, Environmental Technology & Innovation. 14 (2019) 100333 (1–16). https://doi.org/10.1016/j.eti.2019.100333.

[41] S. De Gisi, G. Lofrano, M. Grassi, M. Notarnicola, Characteristics and adsorption capacities of low-cost sorbents for wastewater treatment: A review, Sustainable Materials and Technologies. 9 (2016) 10–40. https://doi.org/10.1016/j.susmat.2016.06.002.

[42] J. Wang, S. Zheng, Y. Shao, J. Liu, Z. Xu, D. Zhu, Amino-functionalized Fe3O4@SiO2 core–shell magnetic nanomaterial as a novel adsorbent for aqueous heavy metals removal, Journal of Colloid and Interface Science. 349 (2010) 293–299. https://doi.org/10.1016/j.jcis.2010.05.010.

[43] L. Sun, S. Hu, H. Sun, H. Guo, H. Zhu, M. Liu, H. Sun, Malachite green Adsorption onto Fe3O4@SiO2-NH2: Isotherms, Kinetic and Process Optimization, RSC Advances. (2012) 11837–11844.

[44] M. Hanif, C.G. Hartinger, Anticancer metallodrugs: where is the next cisplatin?, Future Medicinal Chemistry. 10 (2018) 615–617. https://doi.org/10.4155/fmc-2017-0317.

[45] T. Lazarević, A. Rilak, Ž.D. Bugarčić, Platinum, palladium, gold and ruthenium complexes as anticancer agents: Current clinical uses, cytotoxicity studies and future perspectives, European Journal of Medicinal Chemistry. 142 (2017) 8–31. https://doi.org/10.1016/j.ejmech.2017.04.007.

[46] P. Ferenci, Diagnosis of Wilson disease, in: Handbook of Clinical Neurology, Elsevier, 2017: pp. 171–180. https://doi.org/10.1016/B978-0-444-63625-6.00014-8.

[47] P.C. Panta, C.P. Bergmann, Obtention by Coprecipitation and Magnetic Characterization of Fe3o4 Nanoparticles Coated with Surfactants, Nano Research & Applications. 1 (2015) 1–4.

[48] D.K. Kim, M. Mikhaylova, Y. Zhang, M. Muhammed, Protective Coating of Superparamagnetic Iron Oxide Nanoparticles, Chemistry of Materials. 15 (2003) 1617–1627. https://doi.org/10.1021/cm021349j.

[49] Z. Lu, J. Dai, X. Song, G. Wang, W. Yang, Facile synthesis of Fe3O4/SiO2 composite nanoparticles from primary silica particles, Colloids and Surfaces A: Physicochemical and Engineering Aspects. 317 (2008) 450–456. https://doi.org/10.1016/j.colsurfa.2007.11.020.

[50] D. Dupont, J. Luyten, M. Bloemen, T. Verbiest, K. Binnemans, Acid-Stable Magnetic Core–Shell Nanoparticles for the Separation of Rare Earths, Industrial & Engineering Chemistry Research. 53 (2014) 15222–15229. https://doi.org/10.1021/ie502546c.

[51] G.H. Bogush, C.F. Zukoski, Studies of the kinetics of the precipitation of uniform silica particles through the hydrolysis and condensation of silicon alkoxides, Journal of Colloid and Interface Science. 142 (1991) 1–18. https://doi.org/10.1016/0021-9797(91)90029-8.

[52] Y.A. Barnakov, M.H. Yu, Z. Rosenzweig, Manipulation of the Magnetic Properties of Magnetite−Silica Nanocomposite Materials by Controlled Stober Synthesis, Langmuir. 21 (2005) 7524–7527. https://doi.org/10.1021/la0508893.

[53] M. Zhu, M.Z. Lerum, W. Chen, How To Prepare Reproducible, Homogeneous, and Hydrolytically Stable Aminosilane-Derived Layers on Silica, Langmuir. 28 (2012) 416–423. https://doi.org/10.1021/la203638g.

[54] E.T. Vandenberg, L. Bertilsson, B. Liedberg, K. Uvdal, R. Erlandsson, H. Elwing, I. Lundström, Structure of 3-aminopropyl triethoxy silane on silicon oxide, Journal of Colloid and Interface Science. 147 (1991) 103–118. https://doi.org/10.1016/0021-9797(91)90139-Y.

[55] A. Bayat, M. Shakourian-Fard, N. Ehyaei, M.M. Hashemi, A magnetic supported iron complex for selective oxidation of sulfides to sulfoxides using 30% hydrogen peroxide at room temperature, RSC Adv. 4 (2014) 44274–44281. https://doi.org/10.1039/C4RA07356H.

[56] P. Arévalo-Cid, J. Isasi, F. Martín-Hernández, Comparative study of core-shell nanostructures based on amino-functionalized Fe3O4@SiO2 and CoFe2O4@SiO2 nanocomposites, Journal of Alloys and Compounds. 766 (2018) 609–618. https://doi.org/10.1016/j.jallcom.2018.06.246.

[57] H. Ciftci, B. Ersoy, A. Evcin, Synthesis, Characterization and Cr(VI) Adsorption Properties of Modified Magnetite Nanoparticles, Acta Physica Polonica A. 132 (2017) 564–569. https://doi.org/10.12693/APhysPolA.132.564.

[58] A. Kulpa, J. Ryl, G. Skowierzak, A. Koterwa, G. Schroeder, T. Ossowski, P. Niedziałkowski, Comparison of Cadmium Cd2+ and Lead Pb2+ Binding by Fe2O3@SiO2-EDTA Nanoparticles – Binding Stability and Kinetic Studies, Electroanalysis. 32 (2020) 588–597. https://doi.org/10.1002/elan.201900616.

[59] Y. Liu, R. Fu, Y. Sun, X. Zhou, S.A. Baig, X. Xu, Multifunctional nanocomposites Fe 3 O 4 @SiO 2 -EDTA for Pb(II) and Cu(II) removal from aqueous solutions, Applied Surface Science. 369 (2016) 267–276. https://doi.org/10.1016/j.apsusc.2016.02.043.

[60] S. Jin, B.C. Park, W.S. Ham, L. Pan, Y.K. Kim, Effect of the magnetic core size of amino-functionalized Fe3O4-mesoporous SiO2 core-shell nanoparticles on the removal of heavy metal ions, Colloids and Surfaces A: Physicochemical and Engineering Aspects. 531 (2017) 133–140. https://doi.org/10.1016/j.colsurfa.2017.07.086.

[61] F. Liu, F. Niu, N. Peng, Y. Su, Y. Yang, Synthesis, characterization, and application of Fe3O4@SiO2–NH2 nanoparticles, RSC Adv. 5 (2015) 18128–18136. https://doi.org/10.1039/C4RA15968C.

[62] Y. Zhu, Y. Fang, S. Kaskel, Folate-Conjugated Fe_3O_4@SiO_2 Hollow Mesoporous Spheres for Targeted Anticancer Drug Delivery, The Journal of Physical Chemistry C. 114 (2010) 16382–16388. https://doi.org/10.1021/jp106685q.

[63] S. Shi, J. Yang, S. Liang, M. Li, Q. Gan, K. Xiao, J. Hu, Enhanced Cr(VI) removal from acidic solutions using biochar modified by Fe3O4@SiO2-NH2 particles, Sci. Total Environ. 628–629 (2018) 499–508. https://doi.org/10.1016/j.scitotenv.2018.02.091.

[64] M.E. Khosroshahi, L. Ghazanfari, Synthesis and functionalization of SiO2 coated Fe3O4 nanoparticles with amine groups based on self-assembly, Materials Science and Engineering: C. 32 (2012) 1043–1049. https://doi.org/10.1016/j.msec.2011.09.003.

[65] P.M. Dietrich, S. Glamsch, C. Ehlert, A. Lippitz, N. Kulak, W.E.S. Unger, Synchrotron-radiation XPS analysis of ultra-thin silane films: Specifying the organic silicon, Applied Surface Science. 363 (2016) 406–411. https://doi.org/10.1016/j.apsusc.2015.12.052.

[66] High Resolution XPS of Organic Polymers: The Scienta ESCA300 Database (Beamson, G.; Briggs, D.), J. Chem. Educ. 70 (1993) A25. https://doi.org/10.1021/ed070pA25.5.

[67] S.R. Darmakkolla, H. Tran, A. Gupta, S.B. Rananavare, A method to derivatize surface silanol groups to Si-alkyl groups in carbon-doped silicon oxides, RSC Adv. 6 (2016) 93219–93230. https://doi.org/10.1039/C6RA20355H.

[68] A.K. Chauhan, D.K. Aswal, S.P. Koiry, S.K. Gupta, J.V. Yakhmi, C. Sürgers, D. Guerin, S. Lenfant, D. Vuillaume, Self-assembly of the 3-aminopropyltrimethoxysilane multilayers on Si and hysteretic current–voltage characteristics, Appl. Phys. A. 90 (2008) 581–589. https://doi.org/10.1007/s00339-007-4336-7.

[69] N. Graf, E. Yegen, T. Gross, A. Lippitz, W. Weigel, S. Krakert, A. Terfort, W.E.S. Unger, XPS and NEXAFS studies of aliphatic and aromatic amine species on functionalized surfaces, Surface Science. 603 (2009) 2849–2860. https://doi.org/10.1016/j.susc.2009.07.029.

[70] A. Elhambakhsh, P. Keshavarz, Investigation of Carbon Dioxide Absorption Using Different Functionalized Fe3O4 Magnetic Nanoparticles, Energy Fuels. (2020). https://doi.org/10.1021/acs.energyfuels.0c00234.

[71] Q. Zhao, Y. Zhu, Z. Sun, Y. Li, G. Zhang, F. Zhang, X. Fan, Combining palladium complex and organic amine on graphene oxide for promoted Tsuji–Trost allylation, J. Mater. Chem. A. 3 (2015) 2609–2616. https://doi.org/10.1039/C4TA05205F.

[72] T.L. Barr, S. Seal, Nature of the use of adventitious carbon as a binding energy standard, Journal of Vacuum Science & Technology A: Vacuum, Surfaces, and Films. 13 (1995) 1239–1246. https://doi.org/10.1116/1.579868.

[73] R. Bogdanowicz, M. Sawczak, P. Niedzialkowski, P. Zieba, B. Finke, J. Ryl, J. Karczewski, T. Ossowski, Novel Functionalization of Boron-Doped Diamond by Microwave Pulsed-Plasma Polymerized Allylamine Film, J. Phys. Chem. C. 118 (2014) 8014–8025. https://doi.org/10.1021/jp5003947.

[74] P. Niedziałkowski, R. Bogdanowicz, P. Zięba, J. Wysocka, J. Ryl, M. Sobaszek, T. Ossowski, Melamine-modified Boron-doped Diamond towards Enhanced Detection of Adenine, Guanine and Caffeine, Electroanalysis. 28 (2016) 211–221. https://doi.org/10.1002/elan.201500528.

[75] F. Mirabella, E. Zaki, F. Ivars-Barcelo, S. Schauermann, S. Shaikhutdinov, H.-J. Freund, CO2 Adsorption on Magnetite Fe3O4(111), J. Phys. Chem. C. 122 (2018) 27433–27441. https://doi.org/10.1021/acs.jpcc.8b08240.

[76] J. Pavelec, J. Hulva, D. Halwidl, R. Bliem, O. Gamba, Z. Jakub, F. Brunbauer, M. Schmid, U. Diebold, G.S. Parkinson, A multi-technique study of CO2 adsorption on Fe3O4 magnetite, J. Chem. Phys. 146 (2017) 014701 (1)-014701 (10). https://doi.org/10.1063/1.4973241.

[77] T. Yang, J. Liu, Y. Wang, X. Wen, B. Shen, Structures and energetics of CO2 adsorption on the Fe3O4 (111) surface, Journal of Fuel Chemistry and Technology. 46 (2018) 1113–1120. https://doi.org/10.1016/S1872-5813(18)30044-6.

[78] F. Bai, X. Zhang, X. Hou, H. Liu, J. Chen, T. Yang, Individual and Simultaneous Voltammetric Determination of Cd(II), Cu(II) and Pb(II) Applying Amino Functionalized Fe $_3$ O $_4$ @Carbon Microspheres Modified Electrode, Electroanalysis. 31 (2019) 1448–1457. https://doi.org/10.1002/elan.201900234.

[79] A. Profumo, D. Merli, M. Pesavento, Voltammetric determination of inorganic As(III) and total inorganic As in natural waters, Analytica Chimica Acta. 539 (2005) 245–250. https://doi.org/10.1016/j.aca.2005.02.062.

[80] N. Kataria, V.K. Garg, Green synthesis of Fe3O4 nanoparticles loaded sawdust carbon for cadmium (II) removal from water: Regeneration and mechanism, Chemosphere. 208 (2018) 818–828. https://doi.org/10.1016/j.chemosphere.2018.06.022.

[81] W.H.M. Abdelraheem, Z.R. Komy, N.M. Ismail, Electrochemical determination of Cu2+ complexation in the extract of E. crassipes by anodic stripping voltammetry, Arabian Journal of Chemistry. 10 (2017) S1105–S1110. https://doi.org/10.1016/j.arabjc.2013.01.019.

[82] W. Nowicki, Structural studies of complexation of Cu(II) with aminosilane-modified silica surface in heterogeneous system in a wide range of pH, Applied Surface Science. 469 (2019) 566–572. https://doi.org/10.1016/j.apsusc.2018.11.066.

[83] S.E. Lehman, I.A. Mudunkotuwa, V.H. Grassian, S.C. Larsen, Nano–Bio Interactions of Porous and Nonporous Silica Nanoparticles of Varied Surface Chemistry: A Structural,

Kinetic, and Thermodynamic Study of Protein Adsorption from RPMI Culture Medium, Langmuir. 32 (2016) 731–742. https://doi.org/10.1021/acs.langmuir.5b03997.

[84] D. Chen, T. Awut, B. Liu, Y. Ma, T. Wang, I. Nurulla, Functionalized magnetic Fe3O4 nanoparticles for removal of heavy metal ions from aqueous solutions, E-Polymers. 4 (2016) 313–322. https://doi.org/10.1515/epoly-2016-0043.

[85] M. Sun, P. Li, X. Jin, X. Ju, W. Yan, J. Yuan, X. Changrui, Heavy metal adsorption onto graphene oxide, amino group on magnetic nanoadsorbents and application for detection of Pb(II) by strip sensor, Food and Agricultural Immunology. 29 (2018) 1053–1073. https://doi.org/10.1080/09540105.2018.1509946.

[86] J. Zhang, S. Zhai, S. Li, Z. Xiao, Y. Song, Q. An, G. Tian, Pb(II) removal of Fe3O4@SiO2–NH2 core–shell nanomaterials prepared via a controllable sol–gel process, Chemical Engineering Journal. 215–216 (2013) 461–471. https://doi.org/10.1016/j.cej.2012.11.043.

[87] X.L. Wu, D. Zhao, S.T. Yang, Impact of solution chemistry conditions on the sorption behavior of Cu(II) on Lin’an montmorillonite, Desalination. 269 (2011) 84–91. https://doi.org/10.1016/j.desal.2010.10.046.

[88] J. Vuceta, J.J. Morgan, Hydrolysis of Cu(II)1, Limnology and Oceanography. 22 (1977) 742–746. https://doi.org/10.4319/lo.1977.22.4.0742.